

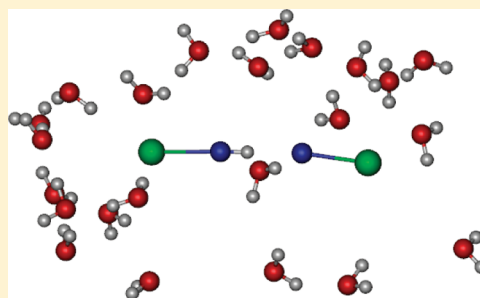
Nonadiabatic Dynamics of Photoinduced Proton-Coupled Electron Transfer: Comparison of Explicit and Implicit Solvent Simulations

Benjamin Auer, Alexander V. Soudackov, and Sharon Hammes-Schiffer*

Department of Chemistry, 104 Chemistry Building, Pennsylvania State University, University Park, Pennsylvania 16802, United States

S Supporting Information

ABSTRACT: Theoretical approaches for simulating the ultrafast dynamics of photoinduced proton-coupled electron transfer (PCET) reactions in solution are developed and applied to a series of model systems. These processes are simulated by propagating nonadiabatic surface hopping trajectories on electron–proton vibronic surfaces that depend on the solute and solvent nuclear coordinates. The PCET system is represented by a four-state empirical valence bond model, and the solvent is treated either as explicit solvent molecules or as a dielectric continuum, in which case the solvent dynamics is described in terms of two collective solvent coordinates corresponding to the energy gaps associated with electron and proton transfer. The explicit solvent simulations reveal two distinct solvent relaxation time scales, where the faster time scale relaxation corresponds to librational motions of solvent molecules in the first solvation shell, and the slower time scale relaxation corresponds to the bulk solvent dielectric response. The charge transfer dynamics is strongly coupled to both the fast and slow time scale solvent dynamics. The dynamical multistate continuum theory is extended to include the effects of two solvent relaxation time scales, and the resulting coupled generalized Langevin equations depend on parameters that can be extracted from equilibrium molecular dynamics simulations. The implicit and explicit solvent approaches lead to qualitatively similar charge transfer and solvent dynamics for model PCET systems, suggesting that the implicit solvent treatment captures the essential elements of the nonequilibrium solvent dynamics for many systems. A combination of implicit and explicit solvent approaches will enable the investigation of photoinduced PCET processes in a variety of condensed phase systems.



I. INTRODUCTION

Photoinduced proton-coupled electron transfer (PCET) reactions play an important role in a variety of biological and chemical systems, including photosynthesis and solar energy conversion devices.^{1–6} Understanding the fundamental physical principles governing such processes is critical for the development of alternative renewable energy sources. Experimental methods have been utilized to study the ultrafast dynamics of photoinduced PCET reactions in solvated molecular systems,^{7–11} in DNA duplexes,^{12,13} and at solution–semiconductor interfaces.^{14,15} The theoretical investigation of these types of processes is challenging because of the quantum mechanical nature of the transferring proton, as well as the strong coupling between the charge transfer dynamics and the solvent dynamics. The calculation of accurate multidimensional excited state potential energy surfaces for charge transfer reactions requires high-level electronic structure methods. Moreover, the additional inclusion of the nuclear quantum effects of the transferring proton and the nonequilibrium solvent dynamics necessitates the development of new theoretical approaches.

Recently, we developed an approach for simulating the nonequilibrium nonadiabatic dynamics of photoinduced PCET reactions based on a dynamical formulation of the multistate continuum theory.^{16–18} In this approach, the PCET complex is represented by an arbitrary number of diabatic electronic states,

and the active electrons and transferring protons are treated quantum mechanically. The electron–proton vibronic free energy surfaces are represented as functions of scalar solvent coordinates corresponding to the energy gaps associated with the single electron and proton transfer reactions involved in the PCET process. The dynamics of the system is governed by a set of coupled generalized Langevin equations of motion describing the time evolution of the collective solvent coordinates, as well as selected intramolecular nuclear coordinates of the PCET complex. The parameters in these Langevin equations depend on the dielectric properties of the solvent, such as the dielectric constants, relaxation times, and molecular moments of inertia. We utilized a surface hopping method^{19,20} to simulate the nonadiabatic Langevin dynamics on the multidimensional electron–proton vibronic free energy surfaces following photoexcitation. This approach enables the description of sequential and concerted mechanisms, as well as more complex branching mechanisms.¹⁸

Implicit solvent approaches based on dielectric continuum models have been shown to be useful in describing the qualitative features of solvation dynamics,^{21,22} as well as the dynamics of chemical reactions in polar solvents.^{23,24} Despite

Received: April 3, 2012

Revised: May 30, 2012

Published: May 31, 2012

the computational efficiency of implicit solvent treatments, however, an explicit molecular representation of the solvent is often necessary to describe the short-time solvent dynamics influenced by the effects from hydrogen-bonding interactions between the solvent and solute and the librational motions in the first solvation shell around the solute.^{25–28} Unfortunately, explicit solvent treatments are computationally expensive and may become prohibitive for systems requiring accurate multidimensional excited state potential energy surfaces. In some cases, implicit solvent treatments may be able to capture the essential physical behavior of the solvent dynamics described in terms of only a few collective solvent coordinates and thereby allow a more accurate treatment of the solute dynamics. Thus, the development of both implicit and explicit solvent approaches is desirable for studying these types of complex nonadiabatic dynamical processes.

The objectives of this paper are to develop an explicit solvent approach for simulating photoinduced PCET reactions, to analyze the new features that arise with an explicit solvent treatment, and to extend the implicit solvent approach to capture these new features. The explicit solvent approach is based on a multistate empirical valence bond (EVB) model,²⁹ in which explicit solvent molecules interact with the PCET complex via a molecular mechanical force field. The transferring proton is treated quantum mechanically, while all other nuclei are treated classically, and the adiabatic electron–proton vibronic states are calculated for each configuration of the classical nuclei sampled during the dynamics. A surface hopping method is used to simulate the nonadiabatic dynamics on multidimensional adiabatic electron–proton potential energy surfaces for vibronic states that are generated on-the-fly. The main advantage of this approach is that the dynamical trajectories are propagated directly on multidimensional potential energy surfaces that include explicit solvent effects, avoiding the choice of specific collective reaction coordinates. The disadvantage of this approach, however, is that it is computationally expensive, even when applied to simple model systems but especially when applied to realistic chemical systems requiring high-level electronic structure methods to generate the excited state potential energy surfaces.

Comparison of the explicit solvent simulations to our previous implicit solvent simulations¹⁸ reveals an important new feature of the PCET dynamics, namely, a faster time scale response of the explicit water molecules in the first solvation shell, in addition to the previously observed slower component corresponding to the relaxation of the bulk solvent. This type of fast femtosecond time scale solvent relaxation associated with the librational motions of the solvent molecules in the first solvation shell was observed previously in studies of solvation dynamics of chromophores in solution.^{25–28} This fast time scale has also been attributed to molecular rotations in the first solvation shell and to inertial motions of the hydroxyl groups in the first solvation shell in previous studies of the solvated electron.^{30,31} Our calculations indicate that the nonadiabatic charge transfer dynamics is strongly coupled to this fast time scale solvent dynamics, leading to a significant decrease in the time scale of the overall charge transfer process when this faster time scale solvent relaxation is included.

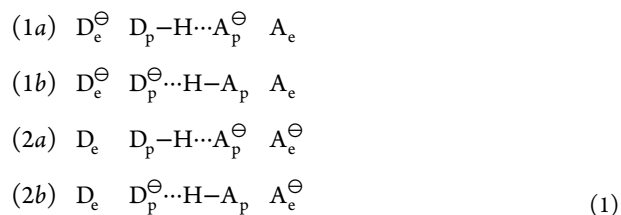
On the basis of the results of our explicit solvent simulations, we extend the dynamical multistate continuum theory to include the effects of two distinct solvent relaxation time scales. The aim of this new implicit solvent approach is to capture the qualitative behavior of the PCET dynamics observed in

simulations with explicit solvent. Comparison of the population dynamics observed in explicit and implicit solvent simulations indicates that the new approach is able to capture both the short-time and long-time relaxation time scales, as well as the coupling between the charge transfer dynamics and the solvent dynamics. For all model systems studied in this paper, the agreement between implicit and explicit solvent treatments is quantitative at short times, and for some models, this quantitative agreement extends to all relevant time scales. For certain models, however, discrepancies are observed at intermediate time scales, indicating limitations of the implicit solvent treatment. Analysis of these models provides insight into the reasons for these discrepancies and possible directions for improvement. In some cases, however, an explicit solvent treatment may be required to capture the subtle interplay among the nonequilibrium solvent dynamics, charge transfer dynamics, and proton vibrational relaxation.

An outline of this paper is as follows. In the first two subsections of Section II, we present the theoretical approach for simulating photoinduced PCET processes with explicit solvent. In the last two subsections of Section II, as well as the Appendix, we present the extension of the dynamical formulation of the multistate continuum theory to include two distinct solvent relaxation time scales for the simulation of photoinduced PCET processes. Section III provides the computational details for the application of these approaches to model systems, including a description of the PCET models, methods for calculating the reorganization energies and solvent parameters of the generalized Langevin equations, methods for simulating the nonadiabatic dynamics, and initial conditions used in the simulations. Section IV presents the results obtained from simulations of photoinduced PCET for a series of model systems using both implicit and explicit solvent methods. The conclusions are summarized in Section V.

II. THEORY

A. PCET Model with Explicit Solvent. The solute complex in the PCET reaction is represented by four diabatic electronic states describing all possible charge transfer states when one electron and one proton are transferred. These four diabatic electronic states are defined in terms of the following four valence bond (VB) states³²



In this notation, ET corresponds to 1→2 and PT corresponds to $a \rightarrow b$. The sequential mechanisms, ET–PT ($1a \rightarrow 2a \rightarrow 2b$) and PT–ET ($1a \rightarrow 1b \rightarrow 2b$), as well as the concerted mechanism, EPT ($1a \rightarrow 2b$), can be described within this framework.

An EVB model is used to construct the potential energy surfaces for the PCET complex immersed in a bath of explicit solvent molecules. The gas phase electronic Hamiltonian of the solute (i.e., PCET complex) is represented in the basis of VB states as

$$H_0^{\text{el}}(\mathbf{r}_p, \mathbf{Q}) = \sum_{i,j}^N h_{ij}(\mathbf{r}_p, \mathbf{Q}) |i\rangle\langle j| \quad (2)$$

where $h_{ij}(\mathbf{r}_p, \mathbf{Q})$ are the matrix elements of the gas phase electronic Hamiltonian in the basis of $N = 4$ diabatic states (i.e., $i, j = 1a, 1b, 2a, 2b$), \mathbf{r}_p is the proton coordinate, and \mathbf{Q} represents the other solute coordinates. The diagonal elements are the potential energy surfaces for the diabatic states, and the off-diagonal elements are the electronic couplings between the diabatic states.

The solvent–solvent and solute–solvent interactions are described by a molecular mechanical (MM) force field. In this case, the total electronic Hamiltonian is

$$H^{\text{el}}(\mathbf{r}_p, \mathbf{Q}, \mathbf{R}) = H_0^{\text{el}}(\mathbf{r}_p, \mathbf{Q}) + \sum_i^N V_i^{\text{ss}}(\mathbf{r}_p, \mathbf{Q}, \mathbf{R}) |i\rangle\langle i| + V^{\text{ss}}(\mathbf{R}) \quad (3)$$

where $V_i^{\text{ss}}(\mathbf{r}_p, \mathbf{Q}, \mathbf{R})$ denotes the solute–solvent interaction for diabatic state $|i\rangle$, $V^{\text{ss}}(\mathbf{R})$ denotes the solvent–solvent interaction energy, and \mathbf{R} denotes the coordinates of the solvent atoms. In our treatment, the transferring proton is treated quantum mechanically. In this context, the electron–proton vibronic Hamiltonian is given by

$$H^{\text{vib}} = T_p + H^{\text{el}}(\mathbf{r}_p, \mathbf{Q}, \mathbf{R}) \quad (4)$$

where the proton kinetic energy operator is $T_p = (-\hbar^2/2m_p)\nabla_p^2$. The adiabatic electron–proton vibronic states can be obtained by diagonalizing the vibronic Hamiltonian given in eq 4 in an appropriate electron–proton vibronic basis. The solute and solvent coordinates, \mathbf{Q} and \mathbf{R} , respectively, can be propagated classically on these adiabatic electron–proton vibronic potential energy surfaces. For the remainder of the paper, we assume that only the solvent coordinates \mathbf{R} are included in the dynamics (i.e., we do not include any additional solute coordinates \mathbf{Q}). The extension of the methodology to include additional solute coordinates is straightforward.

For the purposes of analysis, the energy gap reaction coordinates³³ (i.e., collective solvent coordinates) for PT, ET, and EPT, respectively, are defined as

$$\begin{aligned} Y_{\text{PT}} &= V_{1b}^{\text{ss}}(\mathbf{r}_p, \mathbf{Q}, \mathbf{R}) - V_{1a}^{\text{ss}}(\mathbf{r}_p, \mathbf{Q}, \mathbf{R}) \\ Y_{\text{ET}} &= V_{2a}^{\text{ss}}(\mathbf{r}_p, \mathbf{Q}, \mathbf{R}) - V_{1a}^{\text{ss}}(\mathbf{r}_p, \mathbf{Q}, \mathbf{R}) \\ Y_{\text{EPT}} &= V_{2b}^{\text{ss}}(\mathbf{r}_p, \mathbf{Q}, \mathbf{R}) - V_{1a}^{\text{ss}}(\mathbf{r}_p, \mathbf{Q}, \mathbf{R}) \end{aligned} \quad (5)$$

Note that these reaction coordinates are defined in terms of only the solute–solvent interaction energy and do not include the differences in the gas phase solute energies. Moreover, as will be shown below, the solute–solvent interaction term is defined to be independent of the proton coordinate in our models, so the energy gap reaction coordinates, Y_{PT} , Y_{ET} , and Y_{EPT} , depend only on the solvent coordinates \mathbf{R} .

B. PCET Dynamics with Explicit Solvent. Photoinduced PCET reactions involve nonadiabatic dynamics on multiple adiabatic electron–proton vibronic potential energy surfaces. We use Tully’s fewest switches surface hopping algorithm, also known as molecular dynamics with quantum transitions (MDQTT),^{19,20} to incorporate nonadiabatic transitions between adiabatic potential energy surfaces. In our implementation of the MDQTT method, an ensemble of trajectories is propagated

on the adiabatic electron–proton vibronic surfaces. Each trajectory evolves on a single adiabatic surface but can switch instantaneously to another surface with a probability determined by the quantum amplitudes, which are propagated via the time-dependent Schrödinger equation. The algorithm is designed to ensure that the fraction of trajectories in each state at time t is equal to the quantum probability determined from the quantum amplitudes at time t .

In our implementation of this algorithm, the time-dependent electron–proton wave function $\Psi(t)$ is expanded in a basis of N_{ad} adiabatic electron–proton vibronic states

$$\Psi(t) = \sum_n^{N_{\text{ad}}} C_n(t) \Phi_n(\mathbf{R}) \quad (6)$$

where the adiabatic electron–proton vibronic wave functions $\Phi_n(\mathbf{R})$ with energies $\varepsilon_n(\mathbf{R})$ are obtained by diagonalization of the vibronic Hamiltonian in eq 4 in the electron–proton basis described below. The quantum amplitudes $C_n(t)$ are determined by propagating the time-dependent Schrödinger equation

$$i\hbar \dot{C}_k(t) = \sum_n^{N_{\text{ad}}} C_n(t) [\varepsilon_k(\mathbf{R}) \delta_{nk} - i\hbar \dot{\mathbf{R}} \cdot \mathbf{d}_{kn}(\mathbf{R})] \quad (7)$$

where \mathbf{R} and $\dot{\mathbf{R}}$ are $3N_{\text{solv}}$ -dimensional vectors corresponding to the positions and velocities, respectively, of the N_{solv} solvent atoms, and the $3N_{\text{solv}}$ -dimensional nonadiabatic coupling vectors $\mathbf{d}_{kn}(\mathbf{R})$ are defined as

$$\mathbf{d}_{kn}(\mathbf{R}) = \langle \Phi_k | \nabla_{\mathbf{R}} \Phi_n \rangle = \frac{\langle \Phi_k | \nabla_{\mathbf{R}} H^{\text{vib}} | \Phi_n \rangle}{\varepsilon_n(\mathbf{R}) - \varepsilon_k(\mathbf{R})} \quad (8)$$

The equations for the quantum amplitudes given in eq 7 are integrated simultaneously with the classical equations of motion for the solvent coordinates.

C. PCET Model with Implicit Solvent. In the multistate continuum theory for PCET, the solute complex is represented by the four diabatic states given in eq 1, and the solvent environment is represented by an isotropic and uniform dielectric continuum characterized by a frequency-dependent complex-valued dielectric function $\varepsilon(\omega)$. The solute–solvent interaction is described by the electrostatic interaction of the solute charge distribution with the polarization field of the dielectric continuum, and the solvent dynamics corresponds to the dynamics of the inertial component of the polarization field. In our recent implementation of this theory, the solvent dynamics is described by two coupled generalized Langevin equations (GLEs) of motion describing the time evolution of two collective scalar solvent coordinates related to the energy gaps of the ET and PT processes, respectively.¹⁸ The regular force term in the Langevin equations is obtained from the electron–proton vibronic free energy surfaces, which are functions of the two collective scalar solvent coordinates. The other parameters in the Langevin equations are expressed in terms of the dielectric function and depend on the solvent properties, such as the dielectric constants and dielectric relaxation times. The detailed derivations of these equations are presented elsewhere,¹⁸ and here we summarize only the key aspects directly relevant to the present study.

Previously we derived expressions for the free energy surfaces corresponding to the four diabatic electronic states in eq 1 as functions of two linearly independent collective solvent coordinates, Y_{PT} and Y_{ET} .³² The reaction coordinates Y_{PT} and

Y_{ET} were defined to be the differences in interaction energies of the diabatic charge distributions for the 1a/1b and 1a/2a pairs of diabatic states, respectively, with the inertial polarization field of the solvent. These reaction coordinates are the analogs of the coordinates defined in eq 5 for explicit solvent. In this framework, the diabatic electronic free energy surfaces can be expressed as

$$\begin{aligned} G_{1a}(Y_{PT}, Y_{ET}) &= \frac{1}{2}(\mathbb{T}^{-1})_{11}(Y_{PT} - Y_{PT}^{1a})^2 \\ &+ \frac{1}{2}(\mathbb{T}^{-1})_{22}(Y_{ET} - Y_{ET}^{1a})^2 \\ &+ (\mathbb{T}^{-1})_{12}(Y_{PT} - Y_{PT}^{1a})(Y_{ET} - Y_{ET}^{1a}) \\ G_{1b}(Y_{PT}, Y_{ET}) &= G_{1a}(Y_{PT}, Y_{ET}) + Y_{PT} \\ G_{2a}(Y_{PT}, Y_{ET}) &= G_{1a}(Y_{PT}, Y_{ET}) + Y_{ET} \\ G_{2b}(Y_{PT}, Y_{ET}) &= G_{1a}(Y_{PT}, Y_{ET}) + Y_{PT} + Y_{ET} \end{aligned} \quad (9)$$

where Y_{PT}^{1a} and Y_{ET}^{1a} are the values of the collective solvent coordinates at the minimum of the 1a diabatic free energy surface, and the $[2 \times 2]$ reduced reorganization energy matrix is defined as

$$\mathbb{T} = \begin{pmatrix} 2\lambda_{PT} & 2\lambda_X \\ 2\lambda_X & 2\lambda_{ET} \end{pmatrix} \quad (10)$$

Here λ_{PT} and λ_{ET} are the reorganization energies for PT and ET, respectively, and λ_X is the cross-reorganization energy reflecting the strength of the electrostatic coupling between the PT and ET processes.

In this approach, the electron–proton vibronic free energy surfaces are the eigenvalues of the following surrogate vibronic Hamiltonian

$$\begin{aligned} H^{\text{vib}} &= T_p + \sum_{i,j}^N [h_{ij}(\mathbf{r}_p) + \delta_{ij}G_i(Y_{PT}, Y_{ET})] |i\rangle\langle j|, \\ i, j &= 1a, 1b, 2a, 2b \end{aligned} \quad (11)$$

This vibronic Hamiltonian is the analog of the Hamiltonian defined in eq 4 for explicit solvent. As mentioned above, the eigenvalues are obtained by diagonalization of this Hamiltonian in an appropriate electron–proton vibronic basis. For reasons discussed elsewhere,¹⁸ the solvent dynamics is described in terms of the coordinates $\mathbf{Z} \equiv (Z_p, Z_e)$, which are related to the energy gap coordinates, $\mathbf{Y} \equiv (Y_{PT}, Y_{ET})$, according to the following nonunitary transformation

$$\mathbf{Z} = \mathbb{S}^{-1/2} \mathbb{C}^T [\mathbf{Y} - \mathbf{\Theta}] \quad (12)$$

Here \mathbb{C} is the orthogonal matrix comprised of the eigenvectors of the reorganization energy matrix \mathbb{T} , $\mathbf{\Theta}$ is the column vector with components Y_{PT}^{1a} and Y_{ET}^{1a} , and \mathbb{S} is the diagonal matrix with elements $2f_0\lambda_i$ where λ_i ($i = 1, 2$) are the eigenvalues of the matrix \mathbb{T} , $f_0 = 4\pi\epsilon_0\epsilon_\infty/(\epsilon_0 - \epsilon_\infty)$ is the inverse Pekar factor, and ϵ_0 and ϵ_∞ are the static and optical dielectric constants, respectively. In many cases, Z_p and Z_e are still associated predominantly with the PT and ET interaction energy gaps, respectively.

D. PCET Dynamics with Implicit Solvent. In our previous work,¹⁸ we used the Onodera model of dielectric relaxation³⁴ with a single relaxation time scale and derived the ordinary Langevin equations for the scalar solvent coordinates Z_p and Z_e . The Onodera model accounts for the inertial

behavior of the polarization at short times by introducing corrections to the conventional Debye model. These corrections lead to the acceleration term in the Langevin equation with an effective mass that can be parametrized based on the assumption that the solvent dynamics is described by rotational motion of the individual solvent molecules in the asymptotic limit of high frequencies. To describe the dynamics of photoinduced PCET, we used the MDQT surface hopping method in conjunction with these Langevin equations of motion to simulate the nonadiabatic dynamics on the two-dimensional electron–proton vibronic free energy surfaces following photoexcitation for model systems similar to those studied in the present paper.

As will be shown below, MDQT simulations of photoinduced PCET using explicit solvent molecules reveal that the overall decay of the initial nonequilibrium populations occurs on a significantly shorter time scale than that predicted by our previous simulations based on the multistate continuum model with a single relaxation time scale. Moreover, the MDQT simulations with explicit water molecules exhibit two distinct solvent relaxation time scales. This type of relaxation behavior in water is well-known and has been studied extensively in the context of nonequilibrium solvation dynamics of chromophores in polar solvents.^{25–28} The previous analyses suggest that librational motions of water molecules in the first solvation shell are responsible for the initial fast relaxation on the femtosecond time scale, and collective motions of the bulk solvent molecules are associated with the slower relaxation time scale corresponding to the longitudinal solvent relaxation time on the order of a few picoseconds. In the present paper, we extend the multistate continuum theory to include two solvent relaxation time scales to capture the dynamical behavior observed in simulations with explicit solvent molecules.

Our model is based on the modified Onodera dielectric function with two relaxation time scales

$$\begin{aligned} \epsilon(\omega) &= \epsilon_\infty + \frac{\epsilon_1 - \epsilon_\infty}{(1 - i\omega\tau_2)(1 - i\omega\tau_0)} \\ &+ \frac{\epsilon_0 - \epsilon_1}{(1 - i\omega\tau_1)(1 - i\omega\tau_0)} \end{aligned} \quad (13)$$

where τ_0 is the Onodera free rotational time scale; τ_1 and τ_2 ($\tau_2 \gg \tau_1$) are two dielectric relaxation times; and ϵ_∞ , ϵ_0 , and ϵ_1 are the dielectric constants. This model will be denoted the Onodera-2 model for the remainder of the paper. Note that the Onodera-2 model reduces to the sum of two Debye terms when $\tau_0 = 0$. Using the methodology outlined in our previous paper,¹⁸ we derived the generalized Langevin equations (GLEs) describing the time evolution of two scalar solvent coordinates, Z_p and Z_e , on the two-dimensional free energy surfaces corresponding to the electron–proton vibronic states of the PCET complex in solution. The details of this derivation are provided in Appendix A.

The resulting GLEs have the following form

$$\begin{aligned} \mu\ddot{\mathbf{Z}}(t) + \eta\dot{\mathbf{Z}}(t) - \int_{-\infty}^t \zeta(t - \tau)\dot{\mathbf{Z}}(\tau)d\tau \\ = -\nabla_{\mathbf{Z}}W_n(\mathbf{Z}) - (f_0 + \gamma)\mathbf{Z}(t) + \mathbf{F}(t) \end{aligned} \quad (14)$$

where $W_n(\mathbf{Z})$ is the energy of the n -th electron–proton vibronic state of the PCET solute complex, including the gas phase solute energy and the solute–solvent interaction energy,

f_0 is the inverse Pekar factor, and the exponential friction kernel is given by

$$\zeta(t) = \gamma e^{-t/\tau_\omega} \Theta(t) \quad (15)$$

with $\Theta(t)$ being a Heaviside function. The remaining parameters, μ , η , γ , and τ_ω are expressed in terms of parameters of the Onodera-2 dielectric function given in eq 13, as shown in Appendix A. Finally, $F(t)$ is the Gaussian random force satisfying the fluctuation–dissipation theorem. To enable a comparison between implicit and explicit solvent calculations, the parameters of the GLEs given in eq 14 and the parameters used to generate the electron–proton vibronic surfaces $W_n(\mathbf{Z})$ are determined from equilibrium classical MD simulations of the PCET model systems with explicit solvent molecules, as described in the following section.

III. MODEL SYSTEM CALCULATIONS

A. Model PCET Systems. As in our previous studies,¹⁸ we use a simple five-site model to describe the solute complex. For simplicity, the solute is fixed in space and rigid, and the classical equations of motion are propagated only for the solvent molecules. Thus, the impact of solute dynamics, such as the proton donor–acceptor motion, is neglected in this study. These effects are straightforward to include for future studies of realistic PCET systems. The proton is assumed to move in only one dimension with coordinate r_p along the D_p – A_p axis. Model I is a collinear PCET complex, with the ET and PT donors and acceptors placed along the same axis. For this model, the D_e – A_e distance is 7.5 Å, and the D_p – A_p distance is 2.5 Å. Model II is an orthogonal PCET complex, with the ET and PT donor–acceptor axes perpendicular to each other and bisecting at the midpoints. For this model, the D_e – A_e distance is 6.5 Å, and the D_p – A_p distance is 2.5 Å.

The gas phase potentials for the diabatic states are represented by the sum of a harmonic proton potential, $U_i^{\text{harm}}(r_p)$, an electrostatic Coulomb contribution, U_i^{Coul} , and an energy bias, Δ_i

$$h_{ii}(r_p) = U_i^{\text{harm}}(r_p) + U_i^{\text{Coul}} + \Delta_i \quad (16)$$

The proton potentials, $U_i^{\text{harm}}(r_p)$, are harmonic with a frequency of 3000 cm^{-1} . The minima of the proton potentials for the a and b PT states are positioned symmetrically about the midpoint of the D_p – A_p axis with a separation of 0.5 Å. Note that the proton potentials are chosen to be harmonic for simplicity, but the calculations could be performed with any general proton potential. The electrostatic interaction energy terms, U_i^{Coul} , arise due to the interactions between all pairs of charges on the ET and PT donor and acceptor sites, as given in Table 1. In Model I, the energies of the $|2a\rangle$ and $|1b\rangle$ states are higher than those of the $|1a\rangle$ and $|2b\rangle$ states due to the Coulomb interactions within the solute. To enable a qualitative

comparison to our previous calculations with a dielectric continuum solvent model, we set this energy difference to 30 kcal/mol by adjusting the energy bias, Δ_i . In Model II, all four states have the same electrostatic Coulomb energy because of the orthogonal geometry. For both models, we also consider the effects of the inclusion of an additional energy bias of 23 kcal/mol for the $1a$ and $1b$ states relative to the $2a$ and $2b$ states. Models with this additional energy bias will be indicated by a prime in the nomenclature.

For all models, the electronic couplings between the diabatic states are assumed to be constants. The coupling between the PT diabatic states is $h_{1a,1b} = h_{2a,2b} = 15$ kcal/mol; the coupling between the ET diabatic states is $h_{1a,2a} = h_{1b,2b} = 0.7$ kcal/mol; and the second-order couplings are assumed to be zero (i.e., $h_{1a,2b} = h_{1b,2a} = 0$).

B. Determination of Reorganization Energies. The PT, ET, and EPT reorganization energies can be calculated from MD simulations of the model PCET systems in explicit solvent using the following linear response relations³⁵

$$\lambda_{\text{PT}} = \frac{\langle \delta Y_{\text{PT}}^2 \rangle_{1a}}{2k_B T}, \quad \lambda_{\text{ET}} = \frac{\langle \delta Y_{\text{ET}}^2 \rangle_{1a}}{2k_B T}, \quad \lambda_{\text{EPT}} = \frac{\langle \delta Y_{\text{EPT}}^2 \rangle_{1a}}{2k_B T} \quad (17)$$

where $\delta Y = Y - \langle Y \rangle$ are the fluctuations of the energy gap coordinates, and the angular brackets denote the average over an equilibrium trajectory propagated on the diabatic potential energy surface indicated by the subscript. The cross-reorganization energy λ_X is calculated according to the following relation³²

$$\lambda_X = \frac{1}{2}(\lambda_{\text{EPT}} - \lambda_{\text{PT}} - \lambda_{\text{ET}}) \quad (18)$$

To calculate the reorganization energies, we performed equilibrium MD simulations for Models I and II of the solute and 252 rigid TIP3P³⁶ water molecules in a periodically replicated cubic box with sides of length 19.6616 Å. The 1 ns trajectories were propagated on the potential energy surface corresponding to the diabatic state $1a$, and the energy gap coordinates for each pair of states, as defined in eq 5, were sampled along the trajectory. The average values of the energy gap coordinates and reorganization energies calculated from these MD simulations are given in Table 2.

C. Determination of Parameters of GLE. We explored several different strategies to determine the parameters of the GLEs given in eq 14. The parameters of the dielectric function were fit to reproduce the dielectric properties of bulk water calculated from equilibrium classical MD simulations. The key

Table 2. Average Values of the Interaction Energy Gaps and the Reorganization Energies for PCET Models I and II Calculated from Equilibrium MD Simulations with Explicit Solvent^a

	Model I	Model II
Y_{PT}^{1a}	−1.58	4.60
Y_{ET}^{1a}	19.20	12.95
λ_{PT}	9.02	4.60
λ_{ET}	29.81	12.95
λ_{EPT}	17.63	17.55
λ_X	−10.60	0.0

^aThe units of energy are kcal/mol. Quantities are calculated using eqs 17 and 18 based on the linear response approximation.

Table 1. Charges on Each Site of the PCET Solute Complex for Each Diabatic State in the Explicit Solvent Models^a

	D_e	D_p	H	A_p	A_e
$1a$	− q	q	0	0	0
$1b$	− q	0	0	q	0
$2a$	0	q	0	0	− q
$2b$	0	0	0	q	− q

^aFor Model I, $q = 0.5e$, and for Model II, $q = 0.35e$.

Table 3. Parameter Sets of the Implicit Solvent Models

	O2	O2m		D2 ^a
		Model I	Model II	
ϵ_0	97.4	97.4	97.4	97.4
ϵ_1	95.77	95.61	95.65	95.93
ϵ_∞	1.0	1.0	1.0	1.0
τ_0 , ps	0.003659	0.02173	0.0191	0
τ_1 , ps	0.01715	0.0211	0.0185	0.0185
τ_2 , ps	6.812	6.8132	6.8130	6.8122
μ_p , ps ²	4.223×10^{-4}	0.00277	0.00222	$3.619 \times 10^{-3}/2.336 \times 10^{-3}$
μ_e , ps ²	4.223×10^{-4}	0.00277	0.00222	$1.923 \times 10^{-3}/2.100 \times 10^{-3}$
γ	6.2856	4.3116	4.6120	6.0438
τ_w , ps	0.1203	0.14711	0.14183	0.12246

^aFor the D2 parameter set, all parameters are the same for Models I and II except the effective masses, which are given as Model I/Model II.

quantity that relates the frequency-dependent dielectric function $\epsilon(\omega)$ and the microscopic description of the solvent is the time-dependent total dipole moment $\mathbf{M}(t)$ of the simulation cell and its normalized correlation function, $\phi(t)$

$$\phi(t) = \frac{\langle \mathbf{M}(0) \cdot \mathbf{M}(t) \rangle}{\langle |\mathbf{M}|^2 \rangle} \quad (19)$$

For the case of MD simulations using the Ewald summation technique for treating electrostatic interactions, the following relationships apply between the dielectric function, as well as the associated dielectric constants, and the time-dependent total dipole moment of the simulation cell^{37–40}

$$\frac{\epsilon_0 - \epsilon_\infty}{4\pi} = \frac{\langle |\mathbf{M}|^2 \rangle}{3Vk_B T} \quad (20)$$

$$\frac{\epsilon(\omega) - \epsilon_\infty}{\epsilon_0 - \epsilon_\infty} = \mathcal{L}_{i\omega} \left[-\frac{d\phi}{dt} \right] \quad (21)$$

Here V is the volume of the simulation cell, T is the temperature, and $\mathcal{L}_{i\omega}$ denotes the Fourier–Laplace transform

$$\mathcal{L}_{i\omega}[g(t)] = \int_0^\infty g(t) e^{-i\omega t} dt \quad (22)$$

The Fourier–Laplace transform in eq 21 can be inverted analytically when $\epsilon(\omega)$ is given by eq 13, leading to the following expression

$$\begin{aligned} \phi_{O2}(t) = & 1 - \frac{1}{\epsilon_0 - \epsilon_\infty} \left[\frac{\epsilon_0 - \epsilon_1}{\tau_1 - \tau_0} \tau_1 (1 - e^{-t/\tau_1}) \right. \\ & + \frac{\epsilon_1 - \epsilon_\infty}{\tau_2 - \tau_0} \tau_2 (1 - e^{-t/\tau_2}) \\ & \left. - \left(\frac{\epsilon_0 - \epsilon_1}{\tau_1 - \tau_0} + \frac{\epsilon_1 - \epsilon_\infty}{\tau_2 - \tau_0} \right) \tau_0 (1 - e^{-t/\tau_0}) \right] \end{aligned} \quad (23)$$

The parameters can be obtained by fitting the function $\phi_{O2}(t)$ given in eq 23 to the normalized dipole–dipole time correlation function $\phi(t)$ calculated from an equilibrium MD trajectory for the bulk solvent.

To obtain the data for the total dipole moment of bulk solvent, we performed equilibrium MD simulations for 508 rigid TIP3P water molecules in a periodically replicated cubic box with sides of length 25 Å, treating long-range electrostatic interactions with the Smooth Particle Mesh Ewald (SPME) technique.⁴¹ After an initial 100 ps of equilibration, the

trajectory was propagated for 1 ns with a time step of 1 fs, and the components of the total dipole moment vector of the simulation box were sampled along the trajectory every 10 fs. These data were used to calculate the average value, $\langle |\mathbf{M}|^2 \rangle$, and the time correlation function, $\phi(t)$.

The parameter sets obtained using three different fitting strategies are given in Table 3, and the calculated and fitted dipole–dipole time correlation functions are shown in Figure 1.

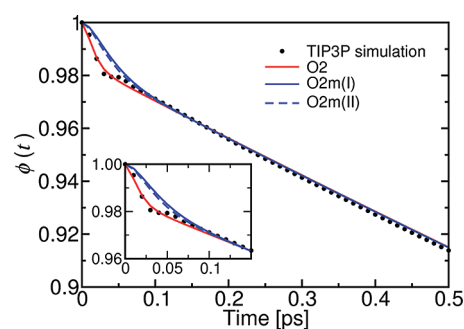


Figure 1. Time correlation function of the total dipole moment obtained from an equilibrium MD simulation of bulk TIP3P water (circles) and fits for the implicit solvent approach with parameter sets O2 (solid red line) and O2m for Model I (solid blue line) and Model II (dashed blue line).

The parameter set denoted O2 was obtained by performing the fit of the Onodera-2 model with only two constraints: $\epsilon_\infty = 1$, corresponding to the nonpolarizable TIP3P water model, and ϵ_0 set to the value of 97.4 determined independently from eq 20. The parameter set denoted O2m was obtained by performing the fit of the Onodera-2 model with the additional constraint of the effective mass μ of the solvent coordinates equated to the average value of the effective masses for the two coordinates, Z_p and Z_e , obtained from equilibrium MD simulations. Specifically, the effective masses were obtained from equilibrium MD simulations of the PCET complex in TIP3P water using the equipartition relations

$$\mu_p \langle \dot{Z}_p^2 \rangle_{1a} = \mu_e \langle \dot{Z}_e^2 \rangle_{1a} = k_B T \quad (24)$$

For the O2m parameter set, the effective mass is constrained to $\mu = (\mu_p + \mu_e)/2$. The parameter set denoted D2 was obtained with the additional constraint of $\tau_0 = 0$. In this case, the Onodera-2 model reduces to the sum of two Debye dielectric functions with relaxation times τ_1 and τ_2 , respectively, and the GLEs lose the acceleration terms due to the vanishing effective

mass. The acceleration terms for the solvent coordinates were then reintroduced into the GLEs by setting the effective masses to the values obtained from the equilibrium MD simulations using eq 24.

For clarity in the figures representing the time-dependent diabatic state populations and average solvent coordinates, we depict only the results obtained with the O2m parameter set. The results obtained with the O2 and D2 parameter sets are similar to those obtained with the O2m parameter set and are provided in the Supporting Information. The advantage of the O2 parameter set is that the generation of these parameters does not require the calculation of the time derivatives of the two energy gap coordinates to obtain the effective masses of these two coordinates, but the disadvantage is that the masses are not consistent with those obtained from the explicit solvent simulations. The advantage of the D2 parameter set is that it has two different effective masses for the two collective solvent coordinates, but the disadvantage is that the analytical connection to the frequency-dependent dielectric function is lost. The O2m parameter set retains this analytical connection while also using effective masses that are more consistent with those obtained from the explicit solvent simulations.

Note that the simulation box used to obtain the total dipole moment data is larger than the simulation box used for the MDQT trajectories. To determine the impact of the box size, we also performed equilibrium MD simulations for 252 rigid TIP3P water molecules in a periodically replicated cubic box with sides of length 19.6616 Å. The resulting parameters are provided in Table S1 of the Supporting Information. Although the parameters are slightly different, the results obtained from MDQT trajectories in implicit solvent with these parameters are qualitatively similar to those presented below for the larger simulation box, which is generally thought to be more accurate. Considering the dependence of the dipole–dipole time correlation function on the size of the simulation box and the choice of periodic boundary conditions, an alternative approach would be to fit the parameters of the dielectric function to reproduce the time correlation functions of the collective solvent coordinates. This approach will be explored in future work. As shown in Figures S1 and S2 of the Supporting Information, however, the time correlation functions of the collective solvent coordinates calculated for the implicit models with the parameters obtained from the dipole–dipole time correlation function are qualitatively reasonable and exhibit time scales and relaxation behavior very similar to those of the time correlation functions calculated from the simulations with explicit solvent.

D. MDQT Simulation Details. Explicit Solvent Model.

The simulations with explicit solvent include one solute complex and 252 water molecules in a periodically replicated cube with sides of length 19.6616 Å. The explicit solvent water molecules are represented with the rigid three-site TIP3P model,³⁶ which includes Lennard-Jones and Coulomb interactions between water molecules. The Lennard-Jones parameters for the electron donor and acceptor sites interacting with the oxygen atoms are chosen to be $\epsilon = 0.153$ kcal/mol and $\sigma = 3.5$ Å. The Lennard-Jones parameters for the proton donor and acceptor sites interacting with the oxygen atoms are chosen to be $\epsilon = 0.15595$ kcal/mol and $\sigma = 3.1416$ Å. Lennard-Jones interactions are not included for hydrogen atoms. The cutoff for the Lennard-Jones interactions is 9.0 Å, and the long-range electrostatic interactions are treated with the SPME method.

The MDQT simulations were performed with a modified version of the DLPROTEIN molecular dynamics simulation package.⁴² The electron–proton vibronic basis functions used to construct the vibronic Hamiltonian in eq 4 were chosen as direct products of the diabatic electronic states and the proton vibrational states corresponding to the proton moving in the gas phase diabatic potentials, $h_{ii}(r_p)$. We used 30 or 50 proton vibrational states for each diabatic electronic state, leading to a total of 120 or 200 electron–proton vibronic basis functions. The one-dimensional proton vibrational wave functions were obtained with the Fourier Grid Hamiltonian method^{43,44} using 64 or 128 grid points for a grid of length 1.5 or 2.5 Å, respectively, along the D_p-A_p axis. The higher number of states and larger grid were used when an electronic bias was applied or the initial proton vibrational wavepacket was shifted.

In the classical MD trajectories, a small time step of 0.025 fs was used to ensure that the results are converged. For equilibration of the initial conditions, the Berendsen thermostat⁴⁵ was used to equilibrate the system to 298 K in the canonical (constant NVT) ensemble. The MDQT trajectories were propagated in the microcanonical (constant NVE) ensemble. A time step that is one-tenth of the classical time step was initially used to integrate the time-dependent Schrödinger equation. When the normalization of the time-dependent wave function differed from unity by more than 10^{-4} , however, the time step was reduced by a factor of 10, and the integration was repeated from the beginning of the classical time step. This process was repeated until the normalization was restored. We propagated 400 surface hopping trajectories for each model system.

The nonadiabatic coupling between the adiabatic electron–proton vibronic states is required for the integration of the time-dependent Schrödinger equation given in eq 7. Use of the chain rule leads to the relation

$$\left\langle \Phi_k \left| \frac{\partial \Phi_n}{\partial t} \right. \right\rangle = \dot{\mathbf{R}} \cdot \mathbf{d}_{kn}(\mathbf{R}) \quad (25)$$

Although the nonadiabatic coupling vector, \mathbf{d}_{kn} , can be computed analytically using eq 8, the analytical calculation of \mathbf{d}_{kn} at each time step of the MD trajectories is computationally expensive. Instead, we calculated the nonadiabatic coupling numerically using a finite difference method to evaluate the derivative of the wave function with respect to time²⁰

$$\begin{aligned} & \left\langle \Phi_k(t + \Delta/2) \left| \frac{\partial \Phi_n}{\partial t}(t + \Delta/2) \right. \right\rangle \\ & \approx \frac{1}{2\Delta} [\langle \Phi_k(t) | \Phi_n(t + \Delta) \rangle - \langle \Phi_k(t + \Delta) | \Phi_n(t) \rangle] \end{aligned} \quad (26)$$

where Δ is the classical time step.

When a switch between two adiabatic states is performed, the nonadiabatic coupling vector must be calculated analytically using eq 8 to adjust the velocities of the solvent atoms to maintain energy conservation. As described in ref 20, the velocities are adjusted as if they were subject to a force in the direction of the nonadiabatic coupling vector. In the present simulations, the MM force field includes constraints because the water is described with a rigid, three-site model. To ensure that the adjusted velocities satisfy the requisite constraints, the velocities must be adjusted with an iterative procedure equivalent to the velocity part of the RATTLE algorithm.⁴⁶ In this paper, we used a straightforward iterative extension of

the procedure described in ref 20 for the velocity adjustment in the presence of constraints. This procedure ensures that the new velocities have no components along the directions of the constrained solvent bonds. For both the explicit and implicit solvent simulations, the system remained in the initial quantum state without any velocity adjustment when there was not enough velocity in the direction of the nonadiabatic coupling vector to maintain energy conservation.

Implicit Solvent Model. For calculation of the vibronic free energy surfaces with the implicit solvent model, we used the same type of electron–proton vibronic basis with 50 proton vibrational states for each diabatic electronic state, leading to a total of 200 electron–proton basis functions. The proton vibrational states were defined on a grid of 128 points spanning 1.7 or 2.6 Å (for models with the shifted initial proton vibrational wavepacket) along the proton donor–acceptor axis. The GLEs given in eq 14 were propagated with a time step of 0.025 fs. The numerical propagation was based on the transformed GLEs given in eq A23 and was performed in the four-dimensional space comprised of the two dynamical solvent coordinates, Z_p and Z_e , and two additional auxiliary coordinates, y_p and y_e , using a combination of second-order Ciccotti⁴⁷ and Honeycutt⁴⁸ integrators. The standard MDQT algorithm described previously^{16,18,20} was used to generate 500 trajectories for each model.

Diabatic State Populations. The MDQT method provides information about the time evolution of the adiabatic state populations and the solvent coordinates for an ensemble of trajectories. As pointed out previously,^{18,49} the diabatic state populations depend on coherences that are not readily available with the MDQT method. To determine the approximate populations of the diabatic states along the trajectories, however, we used the following procedure. We calculated the expectation value of the projectors $\hat{P}_i = |i\rangle\langle i|$ on the diabatic electronic states i for the occupied adiabatic electron–proton vibronic state, summed over the proton vibrational basis states, and assigned the occupied adiabatic state to the diabatic state with the highest expectation value. In general, the operators \hat{P}_i are not diagonal in the adiabatic basis; however, typically the off-diagonal elements are relatively small, so this assignment procedure is physically reasonable except in narrow regions near avoided crossings.

E. Initial Conditions. In the MDQT method, both the initial quantum state and the initial classical coordinates must be specified. We chose the initial quantum state such that it is a direct product of the $|1a\rangle$ diabatic electronic state and the proton vibrational wave function $|\mu_0\rangle$ corresponding to the ground proton vibrational state of the ground electronic state. As in previous studies with a dielectric continuum solvent, we assume that the ground electronic state is not included in the dynamics following photoexcitation. At the start of each trajectory, the initial state is expanded in a basis of the adiabatic electron–proton vibronic states $|n\rangle$

$$|\Psi(t=0)\rangle = |1a\rangle|\mu_0\rangle = \sum_n c_n^0 |n\rangle, \quad c_n^0 = \langle n||1a\rangle|\mu_0\rangle \quad (27)$$

The initial adiabatic state for each trajectory is determined by a procedure in which each adiabatic state $|n\rangle$ is sampled with a probability $|c_n^0|^2$.

The photoexcitation from the ground state is assumed to be instantaneous. We consider two possible ground state proton vibrational wave functions that differ in the position of the minimum of the proton potential, $r_p^{(0)}$, in the ground electronic

state relative to the excited electronic states. In initial condition A, the minimum of the proton potential in the ground electronic state is the same as that in the $|1a\rangle$ diabatic state. For initial condition B, the minimum of the proton potential is halfway between the minima of the proton potentials in the $|1a\rangle$ and $|1b\rangle$ diabatic states. Prior to photoexcitation, we assume that the system is in the ground proton vibrational state of the ground electronic state. For initial condition A, the system is in the ground proton vibrational state of the $|1a\rangle$ diabatic electronic state following photoexcitation. For initial condition B, however, the system is in a coherent mixture of proton vibrational states, where the amplitudes are determined by the Franck–Condon overlaps between $|\mu_0\rangle$ and the proton vibrational wave functions associated with the $|1a\rangle$ diabatic electronic state.

The initial solvent configurations were chosen consistently for the explicit and implicit solvent calculations. For the explicit solvent simulations, the initial solvent configurations were chosen by sampling from an equilibrium classical MD trajectory propagated on a potential energy surface corresponding to a specified diabatic electronic state or mixture of diabatic electronic states. The initial configurations were sampled every 2.5 ps over a 1 ns MD trajectory, leading to 400 configurations. For the implicit solvent calculations, the initial distribution for the two collective solvent coordinates was determined by the average collective solvent coordinates, $Y_{PT}^{(0)}$ and $Y_{ET}^{(0)}$, obtained from the equilibrium classical MD trajectories propagated on the specified diabatic electronic state or mixture of diabatic electronic states. These average coordinates, $Y_{PT}^{(0)}$ and $Y_{ET}^{(0)}$, were transformed to the corresponding average coordinates, $Z_p^{(0)}$ and $Z_e^{(0)}$, using the nonunitary transformation in eq 12. The initial Z_p and Z_e coordinates were sampled from the classical Gaussian distribution associated with the potential of mean force $(1/2)f_0[(Z_p - Z_p^{(0)})^2 + (Z_e - Z_e^{(0)})^2]$ centered at $(Z_p^{(0)}, Z_e^{(0)})$. The initial solvent conditions for the models studied in this paper are presented in Table 4.

Table 4. Initial Conditions

model	$r_p^{(0)}$, Å	$Y_{PT}^{(0)}$, kcal/mol	$Y_{ET}^{(0)}$, kcal/mol
IA(1a/2a)	−0.25	8.565	−11.178
IA(2a)	−0.25	19.626	−40.408
IB(2b)	0.0	1.252	−18.412
IIA(1a/2a)	−0.25	4.6	0.0
IIA(2a)	−0.25	4.6	−12.95
IIB(1b/2b)	0.0	−4.6	0.0

IV. RESULTS

In this section, we present the results obtained from MDQT simulations of photoinduced PCET for the two model systems with various initial conditions using both implicit and explicit solvent approaches. We analyze the time-dependent populations of the four diabatic electronic states representing the PCET system, as well as the time-dependent collective solvent coordinates (i.e., energy gap reaction coordinates). The time-dependent populations reflect the charge transfer dynamics and enable the classification of systems in terms of sequential or concerted PCET mechanisms or in some cases more complex branching mechanisms or cooperative phenomena. The time-dependent solvent coordinates reflect the solvent relaxation dynamics, which can influence the time scale of the overall process through coupling to the charge transfer dynamics.

As will be shown below, our explicit solvent simulations reveal the fast time scale component in the relaxation dynamics of water previously attributed to the librational motions of water molecules in the first solvation shell.²⁷ Moreover, our MDQT simulations of model PCET systems with explicit solvent illustrate that the charge transfer dynamics also exhibit two time scales. The fast time scale of the charge transfer dynamics is on the order of tens of femtoseconds and correlates with the fast time scale of the water relaxation dynamics. In addition, our calculations demonstrate that a carefully designed implicit solvent model is capable of reproducing the results of MDQT simulations with explicit solvent remarkably well.

Figures 2, 3, and 4 depict the results for the collinear model, Model I, which represents a typical PCET system with strong

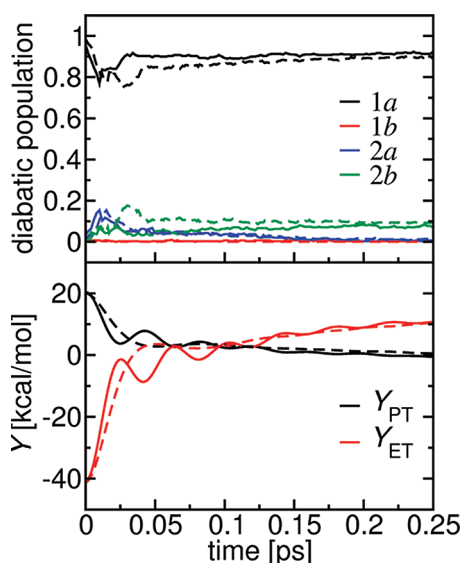


Figure 2. Time-dependent populations of the diabatic electronic states 1a (black), 1b (red), 2a (blue), and 2b (green) in the upper panel and average collective solvent coordinates Y_{PT} (black) and Y_{ET} (red) in the lower panel for Model IA(2a) using the explicit solvent approach (solid lines) and O2m implicit solvent approach (dashed).

electrostatic coupling between the PT and ET interfaces. The dynamics of the populations of the diabatic electronic states for three representative variations of Model I denoted IA(2a), I'A(1a/2a), and IB(2b) are provided in Figures 2, 3, and 4, respectively. The initial solvent configuration is determined from state 2a, an equal mixture of states 1a and 2a, and state 2b for the models depicted in Figures 2, 3, and 4, respectively. An electronic bias is applied only for model I'A(1a/2a), as indicated by the prime, and the initial proton vibrational wavepacket is displaced only for model IB(2b), as indicated by the B. The qualitative mechanisms are illustrated by the dynamics of the diabatic electronic state populations. Figure 2 depicts a PCET process involving only a small degree of concerted EPT. Figure 3 illustrates a branching mechanism that is characterized by fast ET ($1a \rightarrow 2a$) and EPT ($1a \rightarrow 2b$) on the ~ 10 fs time scale, followed by slower PT ($2a \rightarrow 2b$) on the picosecond time scale. Figure 4 illustrates a predominantly concerted EPT ($1a \rightarrow 2b$) mechanism.

Figures 5, 6, and 7 depict the results for the orthogonal model, Model II, which is characterized by the symmetry arising from the vanishing cross-reorganization energy of the PCET process. The dynamics of the populations of the diabatic

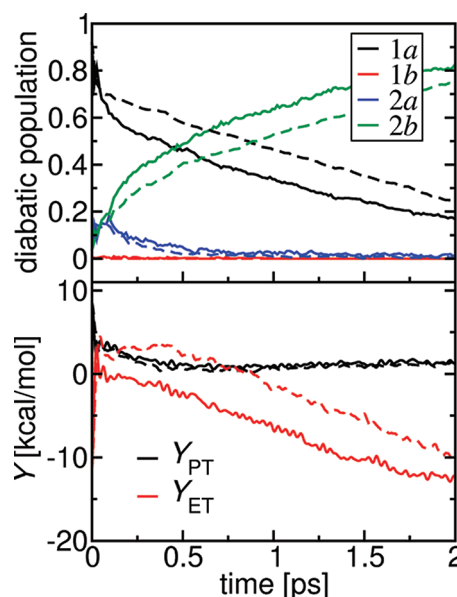


Figure 3. Time-dependent populations of the diabatic electronic states 1a (black), 1b (red), 2a (blue), and 2b (green) in the upper panel and average collective solvent coordinates Y_{PT} (black) and Y_{ET} (red) in the lower panel for Model I'A(1a/2a) using the explicit solvent approach (solid lines) and O2m implicit solvent approach (dashed).

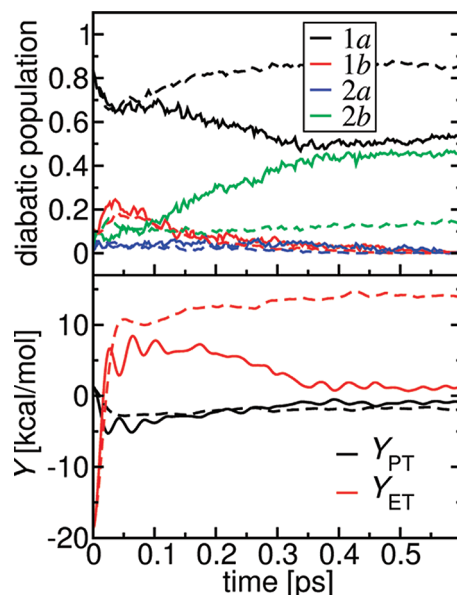


Figure 4. Time-dependent populations of the diabatic electronic states 1a (black), 1b (red), 2a (blue), and 2b (green) in the upper panel and average collective solvent coordinates Y_{PT} (black) and Y_{ET} (red) in the lower panel for Model IB(2b) using the explicit solvent approach (solid lines) and O2m implicit solvent approach (dashed).

electronic states for three representative variations of Model II denoted IIA(1a/2a), IIA(2a), and IIB(1b/2b) are provided in Figures 5, 6, and 7, respectively. The initial solvent configuration is determined from an equal mixture of states 1a and 2a, from state 2a, and from an equal mixture of states 1b and 2b for the models depicted in Figures 5, 6, and 7, respectively. No electronic bias is applied for these models, and the proton vibrational wavepacket was initially displaced in the model denoted IIB(1b/2b). These models correspond to a mixture of sequential and concerted mechanisms that result in

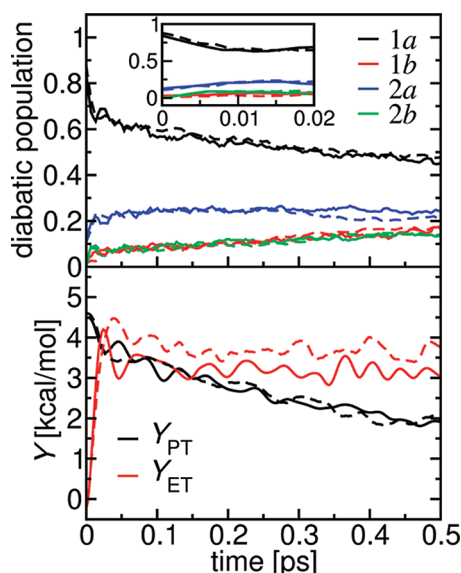


Figure 5. Time-dependent populations of the diabatic electronic states 1a (black), 1b (red), 2a (blue), and 2b (green) in the upper panel and average collective solvent coordinates Y_{PT} (black) and Y_{ET} (red) in the lower panel for Model IIA(1a/2a) using the explicit solvent approach (solid lines) and O2m implicit solvent approach (dashed).

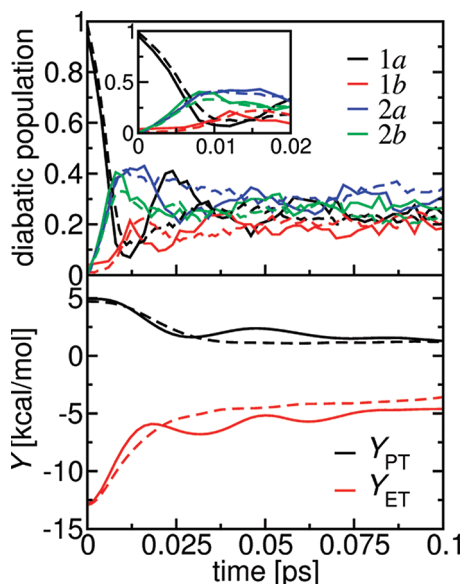


Figure 6. Time-dependent populations of the diabatic electronic states 1a (black), 1b (red), 2a (blue), and 2b (green) in the upper panel and average collective solvent coordinates Y_{PT} (black) and Y_{ET} (red) in the lower panel for Model IIA(2a) using the explicit solvent approach (solid lines) and O2m implicit solvent approach (dashed).

equal populations of all four diabatic electronic states after dynamical relaxation.

In all of these models, the decay of the diabatic electronic state populations clearly exhibits two time scales. The faster time scale is on the order of 10–30 fs and is similar to the fast time scale exhibited in bulk water relaxation. As shown by the time-dependent average collective solvent coordinates, the solvent relaxation dynamics also exhibits two similar time scales. Thus, the charge transfer dynamics during the initial fast decay period is strongly coupled to the fast librational motions of water molecules in the first solvation shell of the PCET

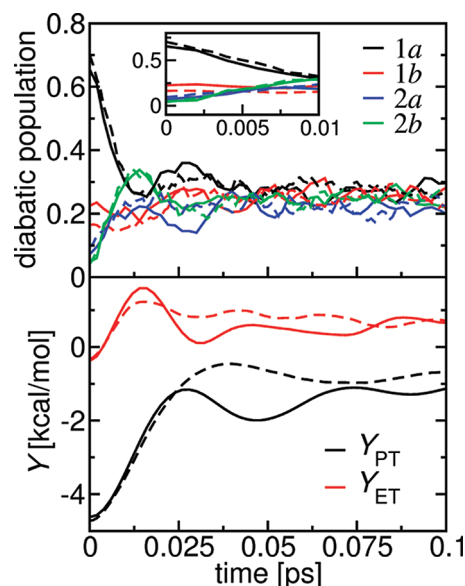


Figure 7. Time-dependent populations of the diabatic electronic states 1a (black), 1b (red), 2a (blue), and 2b (green) in the upper panel and average collective solvent coordinates Y_{PT} (black) and Y_{ET} (red) in the lower panel for Model IIB(1b/2b) using the explicit solvent approach (solid lines) and O2m implicit solvent approach (dashed).

complex. The charge transfer dynamics on the longer time scale is more likely to be coupled to the bulk water relaxation dynamics.

Figures 2–7 depict the results obtained with explicit solvent and with implicit solvent using the O2m parameter set. The results obtained with the other implicit solvent parameter sets are provided in the Supporting Information. In general, the O2m implicit solvent results agreed better with the explicit solvent results, although in the case of the orthogonal model all three implicit solvent parameter sets resulted in virtually identical dynamics. The better agreement for the O2m parameter set than for the O2 parameter set may be attributed to the correct effective mass parametrized to reproduce the inertial dynamics of the PT and ET energy gaps from the explicit solvent equilibrium simulations. The results with the D2 parameter set were nearly identical to those with the O2m parameter set, despite the flexibility to utilize two different masses for the two solvent coordinates in the D2 parameter set. The remainder of this section focuses on comparing the results obtained with implicit solvent using the O2m parameter set to those obtained with explicit solvent.

For all of the model PCET systems studied, the implicit and explicit solvent methods lead to qualitatively similar charge transfer and solvent dynamics, as indicated by a comparison of the time-dependent populations of the diabatic electronic states and the average collective solvent coordinates. The agreement is nearly quantitative for short times, and the diabatic state populations reach equilibrium at longer times (not shown in figures). In the intermediate time regime, however, discrepancies are observed for some of the collinear models. In particular, for the collinear model with the displaced initial proton vibrational wavepacket (Model IB(2b) shown in Figure 4), the diabatic state populations and average solvent coordinates are in nearly quantitative agreement until ~ 0.1 ps. At this time, the explicit solvent calculations branch to a 50/50 mixture of the 1a and 2b states, reaching equilibrium by ~ 0.4 ps, whereas the implicit solvent calculations exhibit less

charge transfer to the $2b$ state and reach equilibrium on a significantly longer time scale. Interestingly, the diabatic state populations obtained from implicit and explicit solvent calculations are virtually indistinguishable for all orthogonal models studied, suggesting that the approximations underlying the implicit solvent method are valid in the limit of weak coupling between the ET and PT interfaces. This agreement also suggests that the implicit solvent approach would work well for single ET or single PT processes with only a single collective reaction coordinate.

The deviations of the diabatic state populations obtained for the collinear model with implicit solvent calculations at intermediate times may be due to several different limitations of the implicit solvent methodology. One limitation is that the implicit solvent models are based on the linear response approximation, resulting in the parabolic shape of the diabatic vibronic free energy surfaces. When the dynamics start far from equilibrium with a significant population of higher vibronic states, as in the case of Model IB($2b$), the nonadiabatic transitions and vibrational relaxation occur in regions where the linear response approximation may not be valid. Moreover, these systems starting far from equilibrium may not be as physically meaningful due to the initial population of highly excited vibronic states for models with harmonic proton potentials.

Another limitation of the implicit solvent methods is related to the neglect of the solute cavity effects that are present in the explicit solvent simulations. For example, in the collinear model, the screening from the solvent is very different for the PT and ET interfaces, leading to slight differences in the dynamics of the PT and ET energy gap reaction coordinates. These differences are manifested in slightly different effective masses for these two coordinates, as extracted from the equilibrium MD simulations with explicit solvent. In the O2m parameter set, the effective masses of the collective solvent coordinates are identical by construction, but in the D2 parameter set, these effective masses are allowed to be different. As shown in the Supporting Information, however, the agreement between implicit and explicit solvent results for the collinear models is not significantly better with the D2 parameter set, suggesting that the use of a single effective mass is not a major cause of the discrepancy. Note that the effective masses of the collective solvent coordinates are very close for the orthogonal model due to the similar solvent environments experienced by the PT and ET interfaces.

A third limitation of the implicit solvent methodology arises from the inherently multidimensional nature of MDQT nonadiabatic dynamics. The stochastic surface hopping algorithm may be significantly influenced by replacing many classical degrees of freedom for the explicit solvent calculations by merely two collective solvent coordinates for the implicit solvent calculations. The models involving strong coupling between the ET and PT interfaces and significant proton vibrational relaxation due to the initial population of highly excited vibronic states are more likely to involve complex coupling among the solvent dynamics, vibrational relaxation, and charge transfer dynamics. This complex coupling may be difficult to capture entirely within a dielectric continuum solvent treatment. In addition, the inadequate treatment of decoherence effects in surface hopping methods may be manifested differently in implicit and explicit solvent calculations. The implicit and explicit solvent results deviate at the time when decoherence effects are expected to become more

important, namely after the initial vibrational relaxation that is followed by a reversal in direction along the collective reaction coordinate and passing through the same avoided crossing regions again. Future work will be directed at exploring methods for including decoherence effects in these types of calculations. Nevertheless, the remarkable qualitative agreement between the implicit and explicit solvent calculations for these PCET models suggests that the MDQT method can be applied in conjunction with implicit solvent models even for solvents with multiple relaxation time scales.

V. CONCLUDING REMARKS

We developed an approach for simulating the ultrafast dynamics of photoinduced PCET reactions in explicit solvent and extended our previously developed implicit solvent approach to describe the two distinct solvent relaxation time scales observed in the explicit solvent simulations. The faster time scale relaxation corresponds to librational motions of solvent molecules in the first solvation shell, while the slower time scale corresponds to the bulk solvent dielectric response. We applied both the implicit and explicit solvent approaches to a series of model systems representing photoinduced PCET. Our calculations illustrate that the charge transfer dynamics is strongly coupled to the fast time scale solvent dynamics associated with librational motions in the first solvation shell, as well as the slower time scale solvent dynamics associated with bulk dielectric relaxation. Specifically, the initial diabatic state population decay occurs on the same time scale as the fast solvent relaxation (i.e., on the ~ 10 – 30 fs time scale), followed by slower charge transfer and solvent dynamics on the ~ 0.1 – 1 ps time scale.

The extended multistate continuum theory approach is able to capture the two distinct solvent relaxation time scales and the coupling between the charge transfer and solvent dynamics. In this approach, the solvent is represented by two scalar collective solvent coordinates corresponding to the energy gaps associated with single ET and PT, respectively. A surface hopping method in conjunction with a set of coupled generalized Langevin equations of motion is used to simulate the nonadiabatic dynamics on the two-dimensional electron–proton vibronic free energy surfaces following photoexcitation. The generalized Langevin equations include two solvent relaxation time scales, as well as a third time scale corresponding to the inertial component of the solvent response. The parameters in these equations can be extracted from equilibrium molecular dynamics simulations of bulk solvent and of the solute immersed in solvent for a single diabatic electronic state. Specifically, the dielectric constants and solvent relaxation time scales are obtained from the time correlation function of the total dipole moment of the simulation cell for bulk solvent; the reorganization energies are obtained from the variances of the two energy gap reaction coordinates; and the effective masses for the two collective solvent coordinates are obtained from the variances of the time derivatives of the two energy gap reaction coordinates.

The implicit and explicit solvent approaches lead to qualitatively similar charge transfer and solvent dynamics for all of the model PCET systems studied. The agreement is quantitative at short times, and the correct equilibrium populations are achieved at longer times; however, discrepancies were observed at intermediate times for some models. Analysis of the cases in which these discrepancies were observed provides insight into the limitations of the implicit

solvent treatment. The collinear and orthogonal models correspond to strong and weak coupling, respectively, between the ET and PT reactions. Excellent quantitative agreement of the diabatic state populations and the solvent dynamics was observed for all orthogonal models studied. The agreement was not as quantitative at intermediate times for the collinear models, particularly for the model involving displacement of the initial proton vibrational wavepacket and hence the initial population of highly excited vibrational states. These discrepancies may be due to the breakdown of the linear response approximation or the neglect of solute cavity effects in the implicit solvent treatment. They may also arise from the inherently multidimensional nature of nonadiabatic dynamics, which cannot be fully captured by a reduced dimensional description in terms of two collective solvent coordinates. Decoherence effects may also be different in multidimensional and reduced dimensional systems.

The effects of the implicit solvent approximations are expected to become more apparent for processes involving complex couplings among the ET and PT charge transfer dynamics, proton vibrational relaxation, and solvent dynamics. These couplings are stronger for the collinear model, and proton vibrational relaxation is more significant when the initial proton vibrational wavepacket is shifted. The quantitative agreement for the orthogonal model suggests that the implicit solvent approach will be even more accurate for processes with only two diabatic electronic states and a single collective reaction coordinate, such as single ET ($1a \rightarrow 2a$) and single PT ($1a \rightarrow 1b$). A comparison of implicit and explicit solvent simulations for these types of systems will be explored in future work. Note that a more accurate force field, such as a polarizable or flexible solvent model, could be utilized and would provide more reliable results. The goal of this paper, however, is to compare implicit and explicit solvent approaches using the same solvent force field to obtain the parameters for the implicit solvent model and to perform the explicit solvent simulations. The effects of more accurate solvent models will be examined in future work.

Overall, the remarkable agreement between the implicit and explicit solvent simulations suggests that the implicit solvent treatment will be adequate for many types of systems. Clearly the explicit solvent approach provides a more detailed description of the nonequilibrium solvent dynamics and is more capable of describing the subtle interplay among the nonequilibrium solvent dynamics, charge transfer dynamics, and proton vibrational relaxation. The significantly greater computational expense of the explicit solvent approach, however, may be prohibitive for some applications, particularly when accurate multidimensional excited state potential energy surfaces are required. In these cases, the implicit solvent treatment may capture the essential elements of the nonequilibrium solvent dynamics, while allowing a more accurate treatment of the solute dynamics. A combination of implicit and explicit solvent approaches will enable the investigation of photoinduced PCET processes in a variety of condensed phase systems.

APPENDIX A

Generalized Langevin Equations Based on the Onodera Model with Two Relaxation Time Scales

In this Appendix, we derive the generalized Langevin equations based on the Onodera model of dielectric relaxation extended

to two relaxation time scales. In this model, the dielectric response function $\varphi(t)$ has the following form

$$\varphi_{O2}(t) = \left[\frac{\varepsilon_1 - \varepsilon_\infty}{\tau_2 - \tau_0} (e^{-t/\tau_2} - e^{-t/\tau_0}) + \frac{\varepsilon_0 - \varepsilon_1}{\tau_1 - \tau_0} (e^{-t/\tau_1} - e^{-t/\tau_0}) \right] \Theta(t) \quad (A1)$$

where τ_0 is the Onodera free rotation time scale; τ_1 and τ_2 ($\tau_2 \gg \tau_1$) are two dielectric relaxation times; ε_∞ , ε_0 , and ε_1 are the dielectric constants; and $\Theta(t)$ is the Heaviside function. The corresponding frequency-dependent dielectric function $\varepsilon(\omega)$ is obtained by the Fourier transform of the response function

$$\begin{aligned} \varepsilon(\omega) &= \varepsilon_\infty + \frac{\varepsilon_1 - \varepsilon_\infty}{(1 - i\omega\tau_2)(1 - i\omega\tau_0)} \\ &\quad + \frac{\varepsilon_0 - \varepsilon_1}{(1 - i\omega\tau_1)(1 - i\omega\tau_0)} \\ &= \varepsilon'(\omega) + i\varepsilon''(\omega) \end{aligned} \quad (A2)$$

The real and imaginary parts of this dielectric function satisfy the Kramers–Krönig relations for generalized susceptibilities

$$\begin{aligned} \varepsilon'(\omega) &= \varepsilon_\infty + \frac{1}{\pi} \mathcal{P} \int_{-\infty}^{\infty} \frac{\varepsilon''(\Omega)}{\Omega - \omega} d\Omega \\ \varepsilon''(\omega) &= -\frac{1}{\pi} \mathcal{P} \int_{-\infty}^{\infty} \frac{\varepsilon'(\Omega) - \varepsilon_\infty}{\Omega - \omega} d\Omega \end{aligned} \quad (A3)$$

The corresponding inverse generalized susceptibility function $f(\omega)$ has the following form

$$\begin{aligned} f(\omega) &= \frac{4\pi\varepsilon(\omega)\varepsilon_\infty}{\varepsilon(\omega) - \varepsilon_\infty} \\ &= f_0 - \mu\omega^2 - i\eta\omega + \gamma - \frac{\gamma}{1 - i\tau_a\omega} \end{aligned} \quad (A4)$$

where $f_0 = f(0) = 4\pi\varepsilon_0\varepsilon_\infty/(\varepsilon_0 - \varepsilon_\infty)$, and the parameters μ , η , τ_a and γ are expressed in terms of the parameters of the dielectric function

$$\mu = \frac{4\pi\varepsilon_\infty^2\tau_0\tau_1\tau_2}{\Delta_2\tau_1 + \Delta_1\tau_2} \quad (A5)$$

$$\eta = \frac{4\pi\varepsilon_\infty^2[\Delta_2(\tau_0 + \tau_2)\tau_1^2 + \Delta_1(\tau_0 + \tau_1)\tau_2^2]}{[\Delta_2\tau_1 + \Delta_1\tau_2]^2} \quad (A6)$$

$$\tau_a = \frac{\Delta_2\tau_1 + \Delta_1\tau_2}{\Delta_1 + \Delta_2} \quad (A7)$$

$$\gamma = \frac{4\pi\varepsilon_\infty^2\Delta_1\Delta_2(\tau_1 - \tau_2)^2(\tau_a - \tau_0)}{[\Delta_2\tau_1 + \Delta_1\tau_2]^3} \quad (A8)$$

with

$$\begin{aligned} \Delta_1 &= \varepsilon_0 - \varepsilon_1 \\ \Delta_2 &= \varepsilon_1 - \varepsilon_\infty \end{aligned} \quad (A9)$$

The inverse Fourier transform of the function $f(\omega)$ can be expressed in terms of the first and second derivatives of the Dirac δ -function as

$$f(t) = \mu\delta''(t) + \eta\delta'(t) + (f_0 + \gamma)\delta(t) - \frac{\gamma}{\tau_\alpha} e^{-t/\tau_\alpha} \Theta(t) \quad (\text{A10})$$

For simplicity, we consider the one-dimensional dynamical equation based on a two-state model. The generalization to the two-dimensional case for a four-state model is straightforward. The generalized Langevin equation describing the time evolution of a collective solvent coordinate z is

$$(\hat{f} - f_0)z(t) = -\frac{dW_k(z)}{dz} - f_0 z(t) + F(t) \quad (\text{A11})$$

where W_k is the energy of the k th adiabatic electron–proton vibronic state, including the gas phase solute energy and the solute–solvent interaction energy, $F(t)$ is the random force satisfying the fluctuation-dissipation theorem (FDT), and \hat{f} is a causal integral operator defined via its action on an arbitrary time-dependent function $g(t)$

$$\hat{f}g(t) = \int_{-\infty}^t f(t-\tau)g(\tau)d\tau \quad (\text{A12})$$

The equation of motion corresponding to the integral kernel $f(t)$ given in eq A10 acquires the following form

$$\begin{aligned} \mu\ddot{z}(t) + \eta\dot{z}(t) + \gamma z(t) - \int_{-\infty}^t \zeta(t-\tau)\dot{z}(\tau)d\tau \\ = -\frac{dW_k(z)}{dz} - f_0 z + F(t) \end{aligned} \quad (\text{A13})$$

where the friction kernel is given by

$$\zeta(t) = \gamma e^{-t/\tau_\alpha} \Theta(t) \quad (\text{A14})$$

The generalized Langevin equation in eq A13, which has an exponential memory term, can be split into two ordinary Langevin equations by introducing an additional auxiliary solvent coordinate. Following the prescription introduced in ref 50, we split the function $f(\omega)$ into two components

$$f(\omega) = f_z(\omega) + f_y(\omega) \quad (\text{A15})$$

where

$$\begin{aligned} f_z(\omega) &= -\mu\omega^2 - i\eta\omega + f_0 + \gamma \\ f_y(\omega) &= -\frac{\gamma}{1 - i\tau_\alpha\omega} \end{aligned} \quad (\text{A16})$$

The integral kernel $f(t)$ is therefore split as follows

$$\begin{aligned} f_z(t) &= \mu\delta''(t) + \eta\delta'(t) + (f_0 + \gamma)\delta(t) \\ f_y(t) &= -\frac{1}{\tau_\alpha}\zeta(t) \end{aligned} \quad (\text{A17})$$

Now we can introduce an auxiliary coordinate y and rewrite the equation of motion in the following form

$$\mu\ddot{z}(t) + \eta\dot{z}(t) + \gamma z(t) + \gamma y(t) = -\frac{dW_k}{dz} - f_0 z(t) + F_z(t) \quad (\text{A18})$$

where

$$\gamma y(t) = -\int_{-\infty}^t \zeta(t-\tau)\dot{z}(\tau)d\tau - F_y(t) \quad (\text{A19})$$

and $F(t) = F_z(t) + F_y(t)$. Taking the derivative of eq A19, we obtain

$$\gamma\dot{y}(t) = \frac{1}{\tau_\alpha} \int_{-\infty}^t \zeta(t-\tau)\dot{z}(\tau)d\tau - \frac{\gamma}{\tau_\alpha} z(t) - \dot{F}_y(t) \quad (\text{A20})$$

Further algebraic manipulations lead to the following equation of motion for the auxiliary coordinate y

$$\gamma\tau_\alpha\dot{y}(t) + \gamma z(t) + \gamma y(t) = G_y(t) \quad (\text{A21})$$

where the random force $G_y(t)$ is defined as $G_y(t) = -\tau_\alpha\dot{F}_y(t) - F_y(t)$.

At this point it is convenient to introduce the following effective potential

$$U_{\text{eff}}(z, y) = W_k(z) + \frac{1}{2}\gamma(z+y)^2 + \frac{1}{2}f_0 z^2 + \text{const} \quad (\text{A22})$$

Using this definition, the original generalized Langevin equation of motion given in eq A13 can be written as a system of two coupled ordinary Langevin equations for coordinates z and y

$$\begin{aligned} \mu\ddot{z}(t) + \eta\dot{z}(t) &= -\frac{\partial U_{\text{eff}}(z, y)}{\partial z} + G_z(t) \\ \gamma\tau_\alpha\dot{y}(t) &= -\frac{\partial U_{\text{eff}}(z, y)}{\partial y} + G_y(t) \end{aligned} \quad (\text{A23})$$

where $G_z(t) \equiv F_z(t)$. The random forces $G_z(t)$ and $G_y(t)$ have no cross-correlation, and the corresponding time-correlation functions satisfy the FDT

$$\begin{aligned} \langle G_z(t)G_z(t') \rangle &= 2k_B T \eta \delta(t-t') \\ \langle G_y(t)G_y(t') \rangle &= 2k_B T \gamma \delta(t-t') \\ \langle G_z(t)G_y(t') \rangle &= \langle G_y(t)G_z(t') \rangle = 0 \end{aligned} \quad (\text{A24})$$

■ ASSOCIATED CONTENT

● Supporting Information

Figures depicting the time correlation functions of the collective solvent coordinates and the corresponding velocities with explicit solvent and with the O2, O2m, and D2 implicit solvent parameter sets for Models I and II; analogs of Figures 2–7 including the results with explicit solvent and with the O2, O2m, and D2 implicit solvent parameter sets; analog of Table 3 using a smaller simulation box. This material is available free of charge via the Internet at <http://pubs.acs.org>.

■ AUTHOR INFORMATION

Corresponding Author

*E-mail: shs@chem.psu.edu.

Notes

The authors declare no competing financial interest.

■ ACKNOWLEDGMENTS

This material is based upon work supported by the Air Force Office of Scientific Research under AFOSR Award No. FA9550-10-1-0081 and NSF Grant CHE-10-57875.

■ REFERENCES

- (1) Hoganson, C. W.; Lydakis-Simantiris, N.; Tang, X.-S.; Tommos, C.; Warncke, K.; Babcock, G. T.; Diner, B. A.; McCracken, J.; Styring, S. *Photosynth. Res.* **1995**, *46*, 177–184.
- (2) Gratzel, M. *Nature* **2001**, *414*, 338.

- (3) Alstrum-Acevedo, J. H.; Brennaman, M. K.; Meyer, T. J. *Inorg. Chem.* **2005**, *44*, 6802–6827.
- (4) Sproviero, E. M.; Gascon, J. A.; McEvoy, J. P.; Brudvig, G. W.; Batista, V. S. *Curr. Opin. Struct. Biol.* **2007**, *17*, 173–180.
- (5) Magnuson, A.; Anderlund, M.; Johansson, O.; Lindblad, P.; Lomoth, R.; Polivka, T.; Ott, S.; Stensjo, K.; Styring, S.; Sundstrom, V.; Hammarstrom, L. *Acc. Chem. Res.* **2009**, *42*, 1899–1909.
- (6) Gust, D.; Moore, T. A.; Moore, A. L. *Acc. Chem. Res.* **2009**, *42*, 1890–1898.
- (7) Cukier, R. I.; Nocera, D. G. *Annu. Rev. Phys. Chem.* **1998**, *49*, 337–369.
- (8) Concepcion, J. J.; Brennaman, M. K.; Deyton, J. R.; Lebedeva, N. V.; Forbes, M. D. E.; Papanikolas, J. M.; Meyer, T. J. *J. Am. Chem. Soc.* **2007**, *129*, 6968–6969.
- (9) Irebo, T.; Reece, S. Y.; Sjodin, M.; Nocera, D. G.; Hammarstrom, L. *J. Am. Chem. Soc.* **2007**, *129*, 15462–15464.
- (10) Gagliardi, C. J.; Westlake, B. C.; Kent, C. A.; Paul, J. J.; Papanikolas, J. M.; Meyer, T. J. *Coord. Chem. Rev.* **2010**, *254*, 2459–2471.
- (11) Westlake, B. C.; Brennaman, M. K.; Concepcion, J. J.; Paul, J. J.; Bettis, S. E.; Hampton, S. D.; Miller, S. A.; Lebedeva, N. V.; Forbes, M. D. E.; Moran, A. M.; Meyer, T. J.; Papanikolas, J. M. *Proc. Natl. Acad. Sci. U.S.A.* **2011**, *108*, 8554–8558.
- (12) de La Harpe, K.; Crespo-Hernandez, C. E.; Kohler, B. J. *Am. Chem. Soc.* **2009**, *131*, 17557–17559.
- (13) Kumar, A.; Sevilla, M. D. *Chem. Rev.* **2010**, *110*, 7002–7023.
- (14) Li, B.; Zhao, J.; Onda, K.; Jordan, K. D.; Yang, J.; Petek, H. *Science* **2006**, *311*, 1436–1440.
- (15) Prezhdo, O. V.; Duncan, W. R.; Prezhdo, V. V. *Acc. Chem. Res.* **2008**, *41*, 339–348.
- (16) Hazra, A.; Soudackov, A. V.; Hammes-Schiffer, S. J. *Phys. Chem. B* **2010**, *114*, 12319–12332.
- (17) Hazra, A.; Soudackov, A. V.; Hammes-Schiffer, S. J. *Phys. Chem. Lett.* **2011**, *2*, 36–40.
- (18) Soudackov, A. V.; Hazra, A.; Hammes-Schiffer, S. J. *Chem. Phys.* **2011**, *135*, 144115.
- (19) Tully, J. C. *J. Chem. Phys.* **1990**, *93*, 1061–1071.
- (20) Hammes-Schiffer, S.; Tully, J. J. *Chem. Phys.* **1994**, *101*, 4657–4667.
- (21) Basilevsky, M. V.; Parsons, D. F.; Vener, M. V. *J. Chem. Phys.* **1998**, *108*, 1103–1114.
- (22) Parsons, D. F.; Vener, M. V.; Basilevsky, M. V. *J. Phys. Chem. A* **1999**, *103*, 1171–1178.
- (23) Malhado, J. P.; Spezia, R.; Hynes, J. T. *J. Phys. Chem. A* **2011**, *115*, 3720–3735.
- (24) Burghardt, I.; Hynes, J. T. *J. Phys. Chem. A* **2006**, *110*, 11411–11423.
- (25) Maroncelli, M.; Fleming, G. A. *J. Chem. Phys.* **1988**, *89*, 5044–5069.
- (26) Roy, S.; Bagchi, B. *J. Chem. Phys.* **1993**, *99*, 9938–9943.
- (27) Jimenez, R.; Fleming, G. R.; Kumar, P. V.; Maroncelli, M. *Nature* **1994**, *369*, 471–473.
- (28) Stratt, R. M.; Cho, M. *J. Chem. Phys.* **1994**, *100*, 6700–6708.
- (29) Warshel, A. *Computer Modeling of Chemical Reactions in Enzymes and Solutions*; John Wiley & Sons, Inc.: New York, 1991.
- (30) Zhu, J.; Cukier, R. I. *J. Chem. Phys.* **1993**, *98*, 5679–5693.
- (31) Barnett, R. B.; Landman, U.; Nitzan, A. *J. Chem. Phys.* **1989**, *90*, 4413–4422.
- (32) Soudackov, A.; Hammes-Schiffer, S. J. *Chem. Phys.* **1999**, *111*, 4672–4687.
- (33) Zusman, L. D. *Chem. Phys.* **1980**, *49*, 295–304.
- (34) Onodera, Y. *J. Phys. Soc. Jpn.* **1993**, *62*, 4104–4107.
- (35) Marcus, R. A. *J. Phys. Chem.* **1989**, *93*, 3078–3086.
- (36) Jorgensen, W. L.; Chandrasekhar, J.; Madura, J. D.; Impey, R. W.; Klein, M. L. *J. Chem. Phys.* **1983**, *79*, 926–935.
- (37) Neumann, M.; Steinhauser, O. *Chem. Phys. Lett.* **1983**, *102*, 508–513.
- (38) Neumann, M.; Steinhauser, O.; Pawley, G. S. *Mol. Phys.* **1984**, *52*, 97–113.
- (39) Neumann, M. *Chem. Phys. Lett.* **1984**, *106*, 563–569.
- (40) Hocht, P.; Boresch, S.; Bitomsky, W.; Steinhauser, O. *J. Chem. Phys.* **1998**, *109*, 4927–4937.
- (41) Darden, T.; York, D.; Pedersen, L. *J. Chem. Phys.* **1993**, *98*, 10089–10092.
- (42) Melchionna, S.; Cozzini, S. *DLPROTEIN*, 2.1 ed.; Cambridge, U.K., 2001.
- (43) Marston, C. C.; Balint-Kurti, G. G. *J. Chem. Phys.* **1989**, *91*, 3571–3576.
- (44) Webb, S. P.; Hammes-Schiffer, S. *J. Chem. Phys.* **2000**, *113*, 5214–5227.
- (45) Berendsen, H. J. C.; Postma, J. P. M.; van Gunsteren, W. F.; DiNola, A.; Haak, J. R. *J. Chem. Phys.* **1984**, *81*, 3684–3690.
- (46) Anderson, H. C. *J. Comput. Phys.* **1982**, *52*, 24–34.
- (47) Vanden-Eijnden, E.; Ciccotti, G. *Chem. Phys. Lett.* **2006**, *429*, 310–316.
- (48) Honeycutt, R. L. *Phys. Rev. A* **1992**, *45*, 600–603.
- (49) Muller, U.; Stock, G. *J. Chem. Phys.* **1997**, *107*, 6230–6245.
- (50) Basilevsky, M. V.; Chudinov, G. E. *Mol. Phys.* **1990**, *71*, 461–476.